

Physics Department
Technical University Federico Santa María

Modern detectors for study Standard Model and Beyond

A thesis presented for the degree of
Doctor of Physics

Abstract

The increased necessity of experimental proof of physics beyond Standard Model (SM) and Dark Matter theories leads us to develop new detectors for high energy experiments, like ATLAS with his upgrade (New Small Wheel project in particular) for the luminosity increase at LHC and a new experiment on SPS facilities at CERN called NA64; to search for Dark Matter on invisible(visible) decays of dark photons.

For this two experiments, detectors from our institute have been made to be part on such enterprise. Characterizations and tests have been done with the use of particles beam (electrons, pions, muons and gamma rays) from the Experimental Area at CERN.

Dedication

Acknowledgments

Agradecimientos

Contents

1. Introduction	13
2. Small-Strip Thin Gap Chamber performance	15
2.1. Introduction	15
2.1.1. High Luminosity Large Hadron Collider	15
2.1.2. ATLAS Detector	16
2.2. small-Strip Thing Gap Chamber	18
2.2.1. Electric field simulation	20
2.2.2. Timming properties	20
2.2.3.	20
2.3. Construction process	20
2.3.1. Quality Control of cathode boards	20
2.3.2. Cathode preparation	21
2.3.3. Graphite spraying	21
2.3.4. Polishing	22
2.3.5. Glue internal parts	22
2.3.6. Winding wires	22
2.3.7. Detector Assembly	22
2.3.8. Planarity and thickness measurements	23
2.4. Gain uniformity measurements	23
2.4.1. Setup	24
2.4.2. Results	24
2.5. Stability under high count rate of γ -rays	27
2.6. Spatial Resolution	28
2.6.1. Analysis Model	29
2.7. Pad efficiency	33
2.8. Summary	36
3. High count rate γ-ray spectroscopy with Brilliance380	37
3.1. Scintillators counters	37
3.2. Counter Limit	37
3.3. Internal radiation	37
3.4. High Radiation Source	37
3.5. Data Analisys	37

3.5.1. Multiple hits	38
3.5.2. Wavelets	38
3.5.3. Peak identification	38
3.6. Results	38
3.6.1. Spectrum	38
3.6.2. Gamma Flux Rates	38
4. Synchrotron Radiation Detector for tagging electrons	39
4.1. NA64 experiment	39
4.1.1. Physics Motivation	39
4.1.2. Dark Photon signal	39
4.1.3. Particle identification	40
4.1.4. Setup	40
4.2. Synchrotron Radiation Detector	40
4.2.1. BGO	40
4.2.2. Pb+Sc	40
4.2.3. LYSO	40
4.3. Calibration	40
4.4. Position and time resolution	40
4.5. Hadron rejection	40
4.6. Purity 100 GeV electron identification	40
4.7. Summary	40
5. Conclusion	41
A. Appendix	43
A.1. Mechanical Measurements sTGC Module 0	43
A.2. PMT RT7525 Data Sheet	43
A.3. Data Structure NA64 Experiment	43
A.4. DAQ system	43

1. Introduction

Let's see if this thing apppear as a introductio

2. Small-Strip Thin Gap Chamber performance

2.1. Introduction

The aim of this chapter is to show the characteristics of the new detectors present on the upgrade for ATLAS detector, and how can achieve the requirements for the high luminosity events. The results of each test to characterize the detector are present.

2.1.1. High Luminosity Large Hadron Collider

The Large Hadron Collider (LHC), run by CERN at the Franco-Swiss border near Geneva, is a circular accelerator with 27km of acceleration pipes, is the largest scientific instrument ever designed and built for scientific research. Successfully commissioned in March 2010 for proton-proton collision with a 7 GeV center-of-mass energy.

The LHC is pushing the limits of human knowledge, enabling physicist to go beyond Standard Model (SM): the enigmatic Higgs boson, mysterious Dark Matter and the world of supersymmetry are just three of the long-awaited mysteries that the LHC will unveil. The announcement given by CERN on 4 July 2012 about the discovery of new boson at 125-126 GeV, almost certainly the long awaited Higgs particle, is the first fundamental discovery, hopefully the first of a series, that the LHC can deliver.

Such discovery was thanks to the different detectors located on the four interaction points; ALICE, LHCb, CMS and ATLAS. This last one is the detector where our university is taking part.

	Period	Energy \sqrt{s}	Luminosity \mathcal{L}	Integrate \mathcal{L}
Run I	2010-2012	7-8 TeV	$6 \times 10^{33} \text{ cm}^{-2}\text{s}^{-1}$	25 fb^{-1}
LS1	2013-2014	Go to design energy, nominal luminosity, bunch spacing	25ns	
Phase 0	2015-2018	14 TeV	$1 \times 10^{34} \text{ cm}^{-2}\text{s}^{-1}$	75 fb^{-1} to 100 fb^{-1}
LS2	2019-2020	Upgrade muon spectrometer;NSW,LAr Calorimeter & FTK		
Phase 1	2021-2023	14 TeV	$2 \times 10^{34} \text{ cm}^{-2}\text{s}^{-1}$	$\sim 350 \text{ fb}^{-1}$
LS3	2024-2025	New Inner Trackker and trigger architecture		
Phase 2	2026-2030	14 TeV	$5 \times 10^{34} \text{ cm}^{-2}\text{s}^{-1}$	$\sim 3000 \text{ fb}^{-1}$

Table 2.1: LHC Schedule

2.1.2. ATLAS Detector

The ATLAS detector is a general-purpose detector, designed to explore proton-proton collisions at center of mass up to $\sqrt{s} = 14\text{ GeV}$ at the Large Hadron Collider (LHC) at the European Laboratory for Particle Physics (CERN). Looking for understand the foundations of matter and forces, in particular the nature of mass in a broad physics programme, including the capability of discovering the Higgs boson over a wide mass range and performing searches for the production of heavy particles that would indicate physics beyond the standard model, such as SUSY particles, as well as searches for other massive objects.

To be able to detect such important and rare events this machine has multiple and complex detector systems. In the central part of this cylinder we have the Inner Detector, the first part of ATLAS to see the decay products of the collisions, so it is very compact and highly sensitive. It consists of three different systems of sensors all immersed in a magnetic field parallel to the beam axis. The **Inner Detector** measures the direction, momentum, and charge of electrically-charged particles produced in each proton-proton collision. The next part is the Calorimeter (red and green on figure 2.1), which measure the energy of a particle when loses its energy as it pass through the detector. It is usually designed to stop entire or “absorb” most of the particles coming from a collision, forcing them to deposit all of their energy within the detector. Calorimeters typically consist of layers of “passive” or “absorbing” high-dense material -for example, lead- interleaved with layers of an “active” medium such as solid lead-glass or liquid argon.

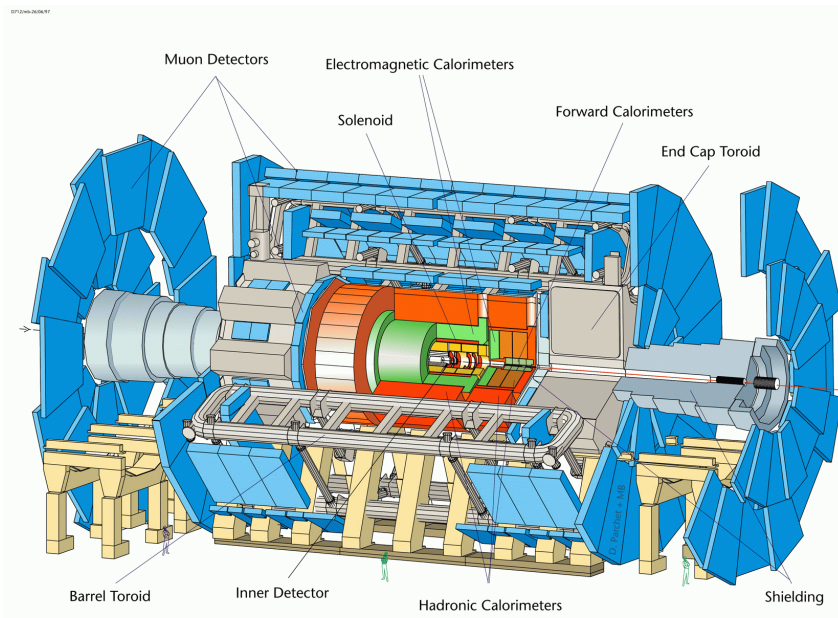


Figure 2.1: ATLAS detector, Muon Spectrometer (in blue)

Electromagnetic calorimeters measure the energy of electrons and photons as they interact with matter. Hadronic calorimeters sample the energy of hadrons (particles

that contain quarks, such as protons and neutrons) as they interact with atomic nuclei. The components of the ATLAS calorimetry system are: the **Liquid Argon (LAr) Calorimeter** and the **Tile Hadronic Calorimeter**.

Calorimeters can stop most known particles except muons and neutrinos. Muons are particles that usually pass through the Inner Detector and Calorimeter undetected, they can penetrate through large amount of material without any strong interaction, they have long lifetime hence offering lepton decay channels for heavy objects as:

For those particles the ATLAS detectors has the **Muon Spectrometer**, made up of 4.000 individual muon chambers (drift chambers) is in charge of identify each one of this muons. This last detector system is a key point to help us finding new physics, thanks that this muons can be considered as a stable particles whithin the volumen range of the ATLAS detector, one can search for products from heavy particles decays to leptons, identifying properly its momentum. Well that part is provided by the **Magnet System**, made of three sections; the **Central Solenoid Magnet** with 2T magnetic field bends the charged particles for momentum measurement near the interaction points, helping the Inner Tracker system, the **Barrel Toroid** bends the particles with low tranversal momentum, and the **Endcap Toroid** with 4T take part of the high tranverse momentum.

Coordinate system

A common coordinate system is used through ATLAS. The interaction point is defined as the origin of the coordinate system. The z-axis runs along the beam line. The x-y plane is perpendicular to the beam line and is referred to as the tranverse momentum, p_T . The positive x-axis points from the interaction point to the de center of the LHC ring; the positive y-axis points upward to the surface of the earth. The detector half at positive z-values is referred to as the “A-side”, to the other half the “C-side”. The transverse plane is often described in terms of $r - \phi$ coordinates. The azimuthal angle ϕ is measured from the x-axis, around the beam. The radial dimension, r , measures the distance from the beam line. The polar angle θ is defined as the angle from the positive z-axis. The polar angle is often reported in terms of pseudorapidity, defined as $\eta = -\ln \tan(\theta/2)$. The distances ΔR is defined in $\eta - \phi$ space as $\Delta R = \sqrt{\Delta\eta^2 + \Delta\phi^2}$.

Detector Upgrade

In manner to fullfill the LHC program (in table 2.1), and in order to benefit from the expected high luminosity performance that will be provided by the Phase-I upgraded LHC, the first station of ATLAS muon end-cap system (Small Wheel, SW) will need to be replaced. The **New Small Wheel (NSW)** will have to operate in a high background radiation region (up to 15 kHz/cm^2 of photons, and 75 Hz/cm^2 of neutrons) while reconstructing muon tracks with high precision as well as furnishing information for the Level-1 trigger. These performance criteria are demanding. In particular, the precision reconstruction of tracks for offline analysis requires a spatial resolution about $100\mu\text{m}$, and the Level-1 trigger track segments have to be reconstructed online with an angular resolution of approximately 1mrad.

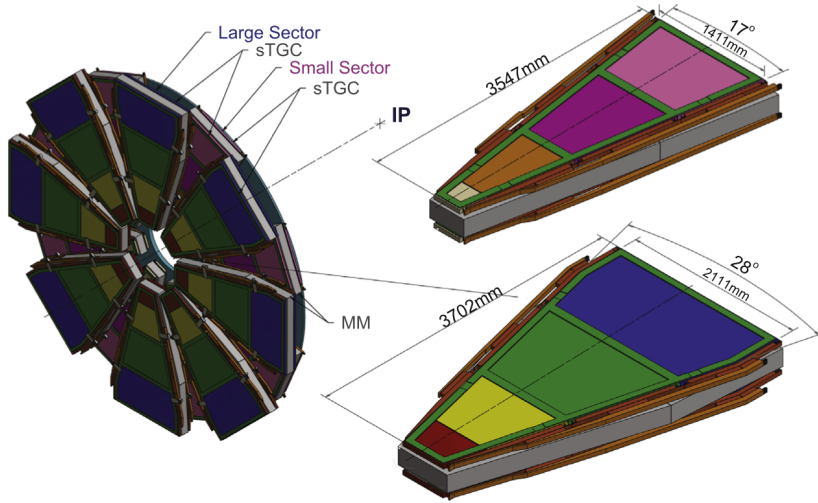


Figure 2.2: New Small Wheel

The NSW will have two chamber technologies, one primarily devoted to the Level-1 trigger function (small-strip Thin Gap Chambers, sTGC) and one dedicated to precision tracking (Micromegas detectors, MM). The sTGC are primarily deployed for triggering given their single bunch crossing identification capability. The MM detectors have exceptional precision tracking capabilities due to their small gap (5mm) and strip pitch (approximately 0.5mm). Such a precision is crucial to maintain the current ATLAS muon momentum resolution in the high background environment of the upgraded LHC. The MM chambers can, at the same time, confirm the existence of a track segments found by the muon end-cap middle station (Big Wheels) online. The sTGC also has the ability to measure offline muon tracks with good precision, so the sTGC-MM chamber technology combination forms a fully redundant detector system for triggering and tracking both for online and offline functions. This detector combination has been designed to be able to also provide excellent performance for the eventual High Luminosity LHC upgrade.

2.2. small-Strip Thing Gap Chamber

The small-Strip Thin Gap Chamber (a.k.a sTGC) detector is a multi-wire proportional chamber (MWPC), a detector type with a relatively old technology, its successful introduction to detector system in 1968 gave the Nobel prize to George Charpak in 1992. Those devices have been a major ingredient in detector system since they can achieve spatial resolution of several microns, and has typical time resolution of about 50ns. The sTGC has been designed to exploit these features, working with a cathode-anode pitch smaller than the anode-anode pitch, mostly based on the design of the Thin Gap Chamber[1], with thinner strips as the main improvement from the previous version. The TGC technology has been used since 1988 in OPAL experiment and currently are part of the the muon spectrometer in ATLAS.

This new chamber has the advantage of having a 3.2mm strip-pitch (2.7mm strips and 0.5mm gap) compare to the 6mm from the previous TGC, that is why the small strip prefix. Chambers with different strips sizes has been build and test under pion beams, chose the 3.2mm as the best option[3] to provide a resolution better than $100\mu\text{m}$. This change will improve the measurement of charge centroid position by charge interpolation.

To improve the time response, the cathode surface resistivity has been reduce by a factor 10, to reduce charge accumulations on the cathode when chamber operates at high rate, lowering from $1\text{ M}\Omega/\square$ to $100\text{-}200\text{k}\Omega/\square$ resistivity on the graphite layer. At the same time cathode-readout plane (strips or pads) distance has been reduce to 0.1mm(1.6mm before) to increase the capacitive coupling by 10, therefore the RC factor keeps unchanged

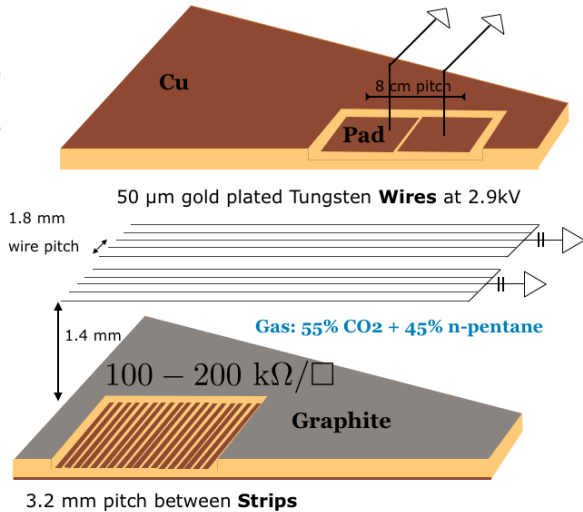


Figure 2.3: Single plane sTGC

The sTGC is made of two resistive cathodes planes, with copper readout plane with strips on one layer and the other one with pads, with $8 \times 12\text{cm}^2$ area used for fast pattern recognition of tracks to select strips for read out. A big advantage compare to the TGC, which has not this feature.

The cathodes are made of FR4 with 1.6mm of thickness, where $100\mu\text{m}$ of copper is etched for strips (pads) and then pressed with a $100\mu\text{m}$ of FR4 over it and then sprayed with graphite to provide for TGC (so it can be treated as a resistive cathode plane). The anodes are golden tungsten wires of $50\mu\text{m}$ diameter, distributed at 1.8mm between each other and a gas gap of 2.8mm. To work with such geometry several test were made to find the proper gas mixture[2]. Find the most suitable mixture of 55% well known carbon dioxide(CO_2) as a quenching gas, and a 45% of n-pentane($\text{n-C}_5\text{H}_{12}$), which allow it to work in a limited proportional region thanks to its capability to absorb UV photons due to its many ways of molecules degree of freedom, vibrational, rotational, etc.

relatively low sensitivity to mechanical variations.[ref Mechanical variations]

2.2.1. Electric field simulation

math explanation of gain dependence of electrical field show countourplot for 5 wires and percentage of high electric field... blind spots!

2.2.2. Timming properties

it has a fast trigger within 25ns of first electrons arrivals.

2.2.3.

2.3. Construction process

Since the main novelty on this detector is the high resolution obtained on xy plane due to the strip boards and the alignment between each chamber to get precision about $50\mu\text{m}$ and $30\mu\text{m}$ respectively, its important to discuss how we achieve those numbers. Everything relies on how well are those chamber built and also how the cathodes boards (strips and pads) are fabricated. The size of each chamber are around 1m^2 to 2m^2 and for the current fabricant it is complicated to achieve $50\mu\text{m}$ resolution etching a pcb board accross 1.5 m without taking into consideration that the standard size for pcb boards are 70 cm long. The attempt of this sections is to give an idea how the sTGC Quadruplets are built, mostly on the first module 0 produce by UTFSM, which is the QS1 (Quadruplet Small sector, part 1). Being the smallest detector to be produce for the NSW, has some pros and cons. The main cons is related to the position of the QS1 inside the NSW, it is the closest one to the interaction point and for that it get the highest rate of particles. For the same reason the position resolution is a key point and the response against high rate particles it is a must. Some pros are related to the size of it, with approximately 1m long and 55 cm the small side and 75 cm the large side of the trapezoidal shape, the sTGC QS1 can be hardly without any problems, its 45 kg at the final step is easy to manage between two people, and with almost 1m long, the etching of strips boards (2.7 mm strip width and 0.5 mm etch) can be achieve with $50\mu\text{m}$.

2.3.1. Quality Control of cathode boards

The cathodes for the module0 were maid by an Italian company MDT, and since it was the first production, the review was done at their place.

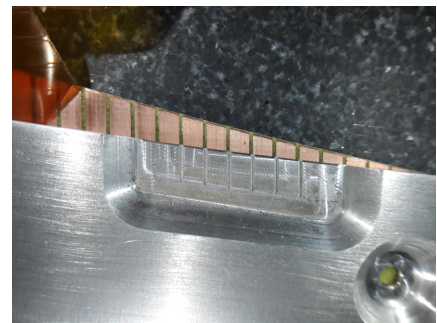
The thickness of the board is measured in 19 points around the perimeter with a micrometer. The values of theses measurments must be whithin $1.6\text{ mm} \pm 25\mu\text{m}$, exceeding this numbers lead to the partial rejection of the cathode boards, however if there is a single point deviation of less than $\pm 35\mu\text{m}$ about the average, it could be used in combination with another cathode board that does not have the same local deviation. The raw data is found in appendix X.

An electrical test is done with a multimeter, to check if there is any short between strips or pads depending on the cathode board.

The last step and the most important is the dimensional control: this must be performed on a flat surface (done on a granite table at the construction site), with 2 pins that match the brass inserts on the cathode and using a special caliper above the cathode board the misalignment is measured. The caliper is an aluminum ruler machining with a precision of $30\ \mu\text{m}$ at 20 Celsius degrees has the same strip pitch for the first and last five strips and to avoid any parallax the thickness is the edge for those strips is 1mm. Looking with a lens glass around this point it is possible to detect some misalignment between these two strips (caliper and cathode board). A photography is taken and analyzed to calculate this misalignment. For such distance (about 1 m long) some precaution must be taken, considering the expansion coefficient for both material. machining with a precision of $30\mu\text{m}$ measure at 20 Celsius degrees.



(a) Al ruler used to check shift over the last strips.



(b) Zoom-in Comparing strip position

2.3.2. Cathode preparation

Once the cathodes pass all the dimensional control are cleaned with Acetone and Isopropyl alcohol and placed on a granite table with a flatness of better than $30\mu\text{m}$, and a vacuum system underneath and fixed on the edges with metal jigs which also has marks for the internal wire support or chamber section. The places which do not need to be sprayed with graphite, like the wire support and the edges are covered with a 3.5m m black tape to the designated wire support locations across the board, and a blue tape the edges preventing spray graphite on the places where they will be glued.

2.3.3. Graphite spraying

A key point for this process is to prepare the 'painting' a mixture of Graphite-33 with Plastik-70 bonding agent. The graphite must be agitated for at least 2 hours before mixing with Plastik-70. A proper ratio of 1500g Graphite and 540g Plastik is mixed for 20min before spraying.

A spraying machine is in charge to get this process done, meanwhile a temperature and humidity must be controlled. After the cathode is painted the superficial resistance is measured on the edges and values above $100\text{k}\Omega/\square$ must get otherwise the cathode needs to be sprayed again.

2.3.4. Polishing

In manner to ensure an uniform resistivity across the chamber, the cathode is visually divide in 5x6 squares. Inside each square the resistivity is measure in 5 to 7 points with a probe and simultaneously brush it in the orientation that the wires will be wound. The brush must be done carefully without over-polish areas because once resistance drops down nothing will bring it back up.

2.3.5. Glue internal parts

After removing all the blue and black tape, all the internal parts such buttons to provide mechanical support to the gas gap, the wire support which help them to not bend due to gravity and create catenary effect, and all the external frames to provide the 1.4mm height for the gas gap. All this part are cleaned with isopropyl alcohol, meanwhile the glue, a type of epoxy (2011-Araldite) is prepared. This glue will not only fix the part, also will fill the surfaces where those part are had less thickness than is requested.

2.3.6. Winding wires

A flat table which can spin around on one axis is used to winding the cathodes board. On each side of the table one cathode with all the internal parts previously glued is mounted and tight it with metal clamps on the edges, meanwhile a vacuum is applied underneath to ensure the flatness of the cathode. A winding machine is in charge of this process, taking all the precautions to place every wire at 1.8mm between each other with **50 μ m precision?**.

After the process is done, all the wires are soldered in group of 10 in the wire rulers with 10M Ω resistor to the high voltage line, later on the remaining wire can be cut and the metal clamps around the edges can be removed.

2.3.7. Detector Assembly

Once the Pad cathode board with all wires soldered is cleaned with clean water and dry with clean air. The board is placed on the granite table, vacuum is applied underneath so it can be ready to connect it to high voltage. It is necessary to monitor the current from the cathode meanwhile the voltage is increased, starting with 100V and reach 3000V, every 100V step the current is monitoring and check that never goes higher than 1 μ A, if it is the case, the cathode needs to watch carefully on each corner to see some small sparks around dust or remaining glue from the previous process.

Reaching the nominal current, the strip cathode board is placed against the pad cathode board carefully, and an aluminum frame with a silicon rubber is placed on top to isolate the chamber from the environment, afterwards the vacuum is applied to this chamber and only CO₂ is flushing inside the chamber. Now it is the time to turn on the power supply and watch if there is no sparks (monitoring the current), if it is not the case, the glue is prepared to close the chamber immediately to prevent any dust enter the chamber

when the silicon rubber and the strip cathode board is remove. Finishing this process, a single chamber detector is considered done.

Closing two chambers is possible build a doublet, for that it is necessary to glue a honeycomb with a well known thickness ($5\pm0.02\text{mm}$)

2.3.8. Planarity and thickness measurements

Total thickness.

2.4. Gain uniformity measurements

After the chambers are built it is important to look for any malfunctioning. To check the behaviour of the detector without any electronic readout attach to strips or wires, is to use a radiation source and move it across the sensitive area and expect the same behaviour current draw from it. This will give us a the first answer of the gain of our detector.

In this test it is important to understand what can produce variation on the gain. There are two ingredients that can produce gain variations on wire detectors, the first one is the "nature" gain fluctuations from the charge production in proportional counters which follow Polya distribution, however is less pronounced in limited-proportional mode such as sTGC working region.

The second one is related to the mechanical tolerances, this part is very well known since 40 years as it is presented on Sauli's book [Insert ref](#) about drift chambers and tell us:

- A diameter variations of the wire about 1% (fabrication precision) will result on a 3% change in the gain.
- $100\mu\text{m}$ difference in the gas gap thickness(2.7mm) results in about 15% change on the gain.
- The effect of a wire displacement of about $100\mu\text{m}$ of a wire plane results in 1% in the charge of the two adjacent wires which with a gain of $\sim 10^6$ will give a $\sim 10\%$ change on the gain.

Taking all of this in consideration is expected to get a gain variation less than 20% as Quality Acceptance on the Construction manual [Insert Ref](#).

In this test the gain is considered as the current draw measured from the power supply and its need to test under two different working points (bias voltage), one when the chamber it is not in the limited proportional region, 2500 volts, a take it as a reference compare to the 2900 volts which is the operational voltage.

For such test the x-ray source is used thanks to the advantages:

- Mostly mono-energetic photons.
- Variable current: which can provides different rates. [$1\mu\text{A} - 200\mu\text{A}$]
- Variable voltage: modifying breaking voltage of electrons inside the x-ray gun. [$10\text{keV} - 50\text{keV}$]

- Different spot size: with a set of collimator it is possible to irradiate only interesting area.
- Portable, it is possible to move across the sensitive area of the detector.

2.4.1. Setup

To perform such test a x-ray gun called Mini-x from Amptek is used, with silver (Ag) as transmission target with a beryllium (Be) end window is used. Working under 50kV with $45\mu\text{A}$, the emission spectra Fig.2.5 show two main photo peaks with 22 and 25 keV. The aperture emissions is about 120 degrees, so a collimator of 5 degrees is placed to provide a spot size of 4mm.

The gun is mounted on a robot arm KUKA, to move it across the detector irradiating a long the wires. Since the high voltage power supply give us a current average per second, the vertical and horizontal step can be adjust to perform a spot size of 4mm^2 however the Mini-x device had some overheat issues so a 5cm vertical step was chosen to perform a full irradiation test in less time. A more suitable step would be 1cm to detect internal structures of similar sizes. The horizontal step was 1.5cm, enough to change completely from group wires, although it will better to improve the granularity it is not possible since the issue explained before.

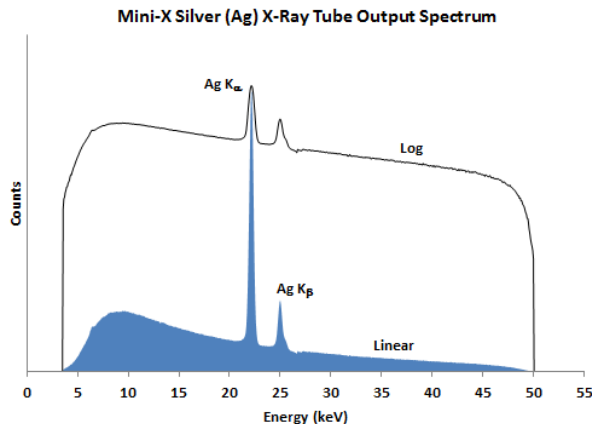


Figure 2.5: X-ray emission spectra from Mini-X gun

The irradiation test is taken in approximately one hour and the four chamber are done at the same time, meanwhile the division of each chamber are connected to the same HV channel.

2.4.2. Results

The next two set of histograms shows the distribution of the current draw at two different voltage, one at 2500V to take it as reference since the chamber can be consider with no gain (no proportional mode), and the second one the voltage at what our chamber must be working 2900V.

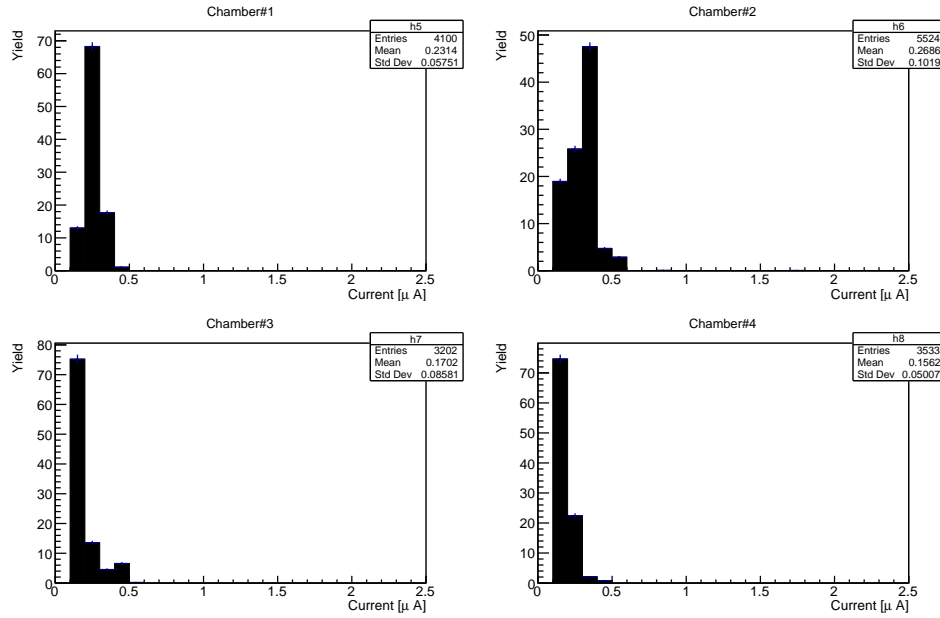


Figure 2.6: Current from power supply at 2500V

On the Figure 2.6 an average of approximately 200nA can be observe on the four layers, considering 50nA when no source is present (leakage current). As previously discuss the important part is to get how uniform are the chambers across the whole sensitivity area, even the places where the internal parts are found, such a wire supports and buttons, which in that case a notoriously decrease of gain (less current draw) is expected due to the lack of gas volume, and so no amplification.

On the Fig2.7 the current draw for each single chamber is shown and an uniformity less than 17% is obteind, calculated as rms percentage over mean.

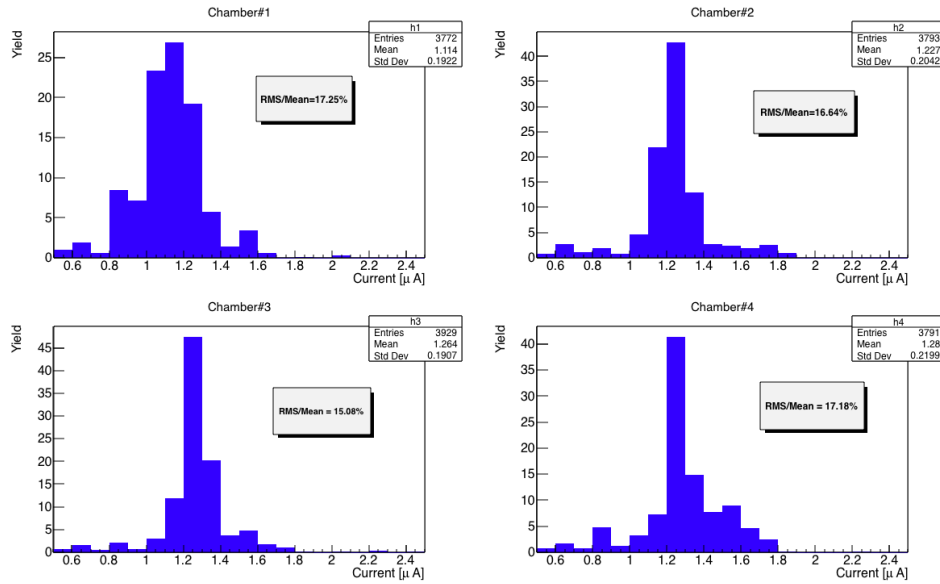


Figure 2.7: Current from power supply at 2900V

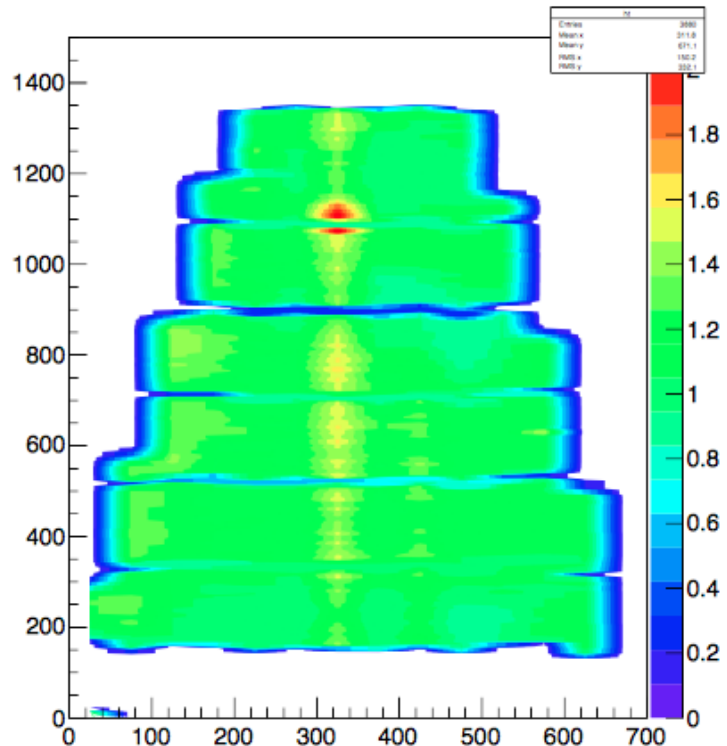


Figure 2.8: XY Scan Layer 3 sTGC Module #0

2.5. Stability under high count rate of γ -rays

One of the key feature of this detector is that must be able to work under high particles flow rates ($15\text{kHz}/\text{cm}^2$), and the first step is check weather the device or its electronic components can handle this high rate. For this purpose the module 0 was placed inside of a High Radiation Facility at CERN called GIF++. The instalation has a Cesium-137 as a gamma source with an activity of approximately 17TBq and different attenuation filters can be applied to get the flux needed. To get the particle rate a small size sTGC was installed as a **Monitor**, which has the electronic readout from each wire group, equipped with the SONY card ([provide description](#)).

Our module 0 together with the monitor was placed at 1.3m distance from the source, both connected in serie to the same gas line, the temperature and pressure was recored to keep in track the working voltage, where most of the time the enviromental conditions were 25 Celsius degree and 971mb .

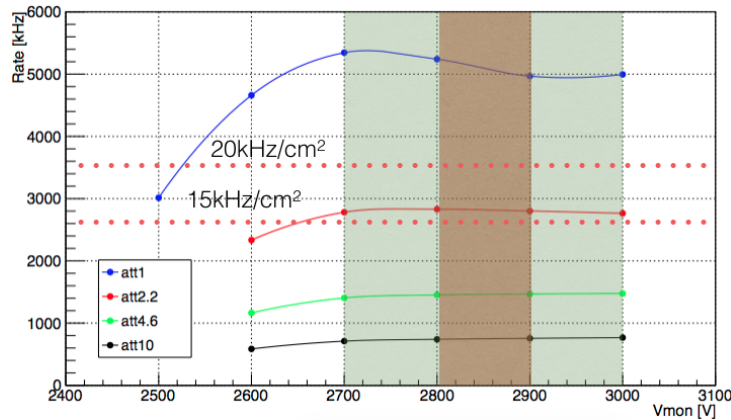


Figure 2.9: Monitor rate

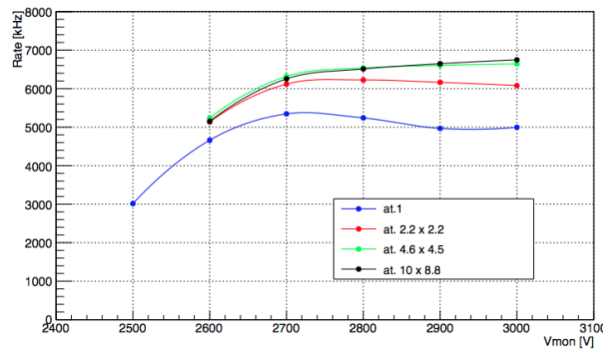


Figure 2.10: Filters applied

On the fig.2.9 the event rate register with the monitor is shown at different attenuation filters from the gamma source, where attenuation 1 means 5TBq . The brown region is

our working region, and the red dot lines are the limits where our chamber must work inside the ATLAS cavern. On fig. 2.10 the event rate is shown applying the attenuation factors which the gamma filters provide, so all the lines must join, however we do see some inefficiency when the rate goes higher than 20kHz/cm (blue line), but at the same time, our interest should go on the red line (attenuation factor of 2.2) which gives us the background level present on the upgrade. If we compare it with lowest rates, the efficiency is about 95% at 2.9kV.

2.6. Spatial Resolution

In order to achieve the precision reconstruction of tracks (offline) with a spatial resolution of about $100\mu\text{m}$ per sTGC layer, and fast trigger on the region of interest (ROI) with Pads, two test beams were done.

In the spring of 2014, the Weizmann Institute of Science in Israel built the first full-size sTGC quadruplet detector of dimensions $1.2 \times 1.0\text{m}^2$. This prototype consists of four sTGC strip and pad layers and is constructed using the full specification of one of the quadruplets to be used in the NSW upgrade (the middle quadruplet of the small sector). The first test beam experiment took place at Fermilab with one goal in mind, determine the position resolution of a full-size sTGC.

par EUDET pixel telescope were used as a reference for measure beam position, using the

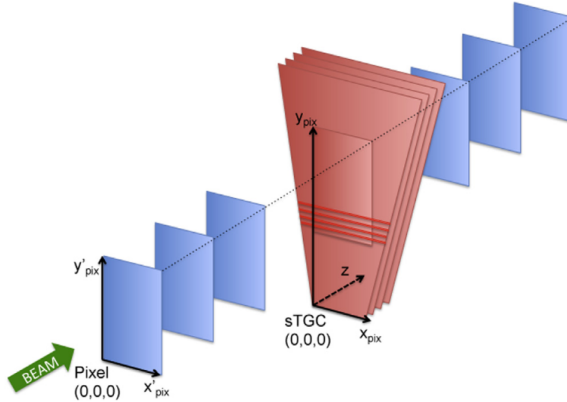


Figure 2.11: Schematic diagram of the experimental setup at Fermilab and coordinate systems used. Three layers of silicon pixel sensors are positioned before and after the sTGC detector. The dimensions are not to scale.

technology of 6 Minimum Ionizing MOS Active Pixel Sensor (Mimosa26) detectors with $\approx 5\mu\text{m}$ position resolution. Three in front of the beam, and three after the sTGC as is shown in fig.2.11 with 15cm between them and 64cm between each arm. Each Mimosa26 detector has an active area of 2.24cm^2 made of CMOS pixel matrix of 576 rows and 1152 columns with $18.4\mu\text{m}$ pitch.

A 32GeV pion beam was used at rate of 1kHz over a spot of 1cm^2 giving to the sTGC a very precise pion trajectory thanks to the EUDET telescope. Event triggering was

controlled by a custom Trigger Logic Unit (TLU). The TLU received signals from two 1x2cm² scintillators placed in front and behind the telescope. The TLU generated the trigger signal that was distributed to the telescope and the sTGC readout electronics, which consist of a first application-specific integrated circuit (ASIC) called VMM1 which has the ability to read out both positive (strips, pads) and negative (wires) polarity signals, on 64 individual readout channel. The VMM1 analog circuit features a charge amplifier stage followed by a shaper circuit and outputs the analog peak value (P) of the signal. The readout of the ASIC is zero suppressed and thus only peak values of channels with signals above a predefined threshold are read and at the same time the VMM1 may be programmed to provide the input signal amplitude of channels adjacent to a channel above threshold (neighbour-enable logic), which in case of the strips is strictly necessary due to the cluster size is about 3-5 strips.

The precise position of a charged particle traversing an sTGC gas volume can be estimated from a Gaussian fit to the measured charge on adjacent readout strips (referred to as strip-clusters from here on). Given the strip pitch of 3.2mm and sTGC geometry, charges are typically induced on up to five adjacent strips. The spatial sampling of the total ionization signal over a small number of readout channels means that a precise knowledge of each individual readout channel baseline is necessary in order to achieve the best possible measured spatial resolution. The baseline of each individual readout channel was measured by making use of the neighbour-enabled logic of the VMM1 and its internal calibration system. Test pulses were sent on one readout channel with the neighbour-enabled logic on, and baseline values were obtained by reading out the analog peak values of the two channels adjacent to the one receiving a test pulse.

The silicon pixel hit positions were then used for reconstructing straight three dimensional charged-particle tracks. A track quality parameter was obtained for each fitted pion track based on the χ^2 of the track-fit. A small value of the track quality parameter corresponds to a straight track and a cut on this parameter can therefore be used to mitigate multiple scattering which are not considered in this analysis.

2.6.1. Analysis Model

Pixel telescope analysis

In this model the intrinsic position resolution is obtained comparing the extrapolated beam trajectory from the pixel detectors with the measurements in each of the sTGC quad planes. Each layer is analyzed separately to reduce the effect of the multiple scattering and only tracks with $\chi^2 < 10$ are considered for the same reason. From fig.2.11 you can see that the y -axis is defined perpendicular to the strips, therefore sTGC strip-clusters provide measurements of the particle position in the y -direction(y_{sTGC}). The position resolution is directly related to the profile of induced charge on the strips. The particle position is estimated from a Gaussian fit to the induced charge distribution on the strips. The neighbour-enabled logic of the VMM1 was used. Strip-clusters with induced charge in either 3, 4 or 5 adjacent strips are selected.

The pixel telescope tracks provide both coordinates, x_{pix} and y_{pix} at the position of

Table 2.2: Fit parameters per cluster size

Strip-cluster multiplicity i	Amplitude parameter a_i
3	205 ± 9
4	206 ± 4
5	211 ± 5

the sTGC layer studied. The spatial resolution measurement is obtained by fitting the residual distribution y_{sTGC} and y_{pix} with a Gaussian model.

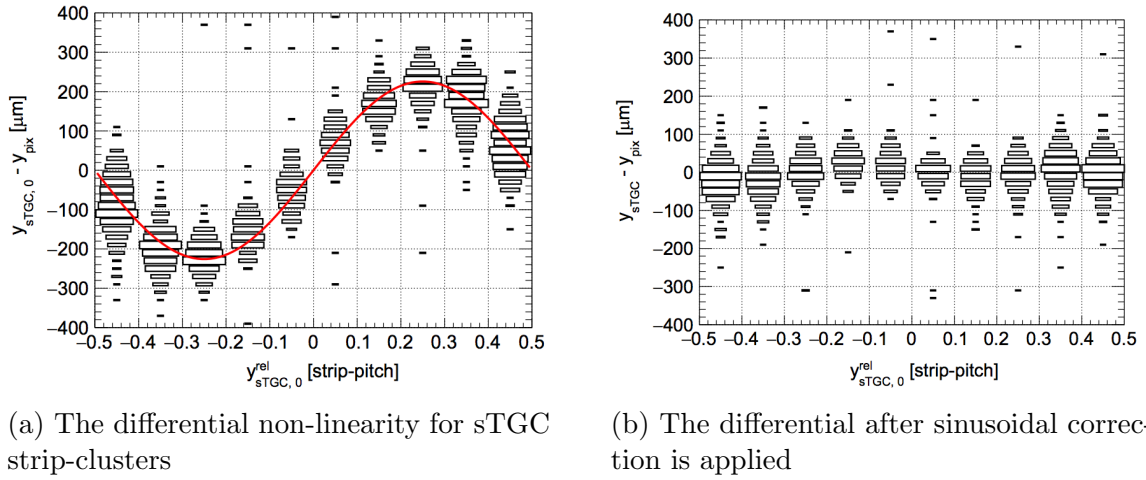


Figure 2.12: Charge distribution over strip-pitch

The charge measured on the strips of the sTGC detector results from a spatial sampling and discretization of the induced charge. The process of reconstructing the sTGC strip-cluster position from this sampling introduces a differential non-linearity effect on the reconstructed strip-cluster position. The deviation of the measured strip-cluster position from the expected position (estimated by the pixel telescope track) depends on the strip-cluster position relative to the strips. This dependence is clearly seen in the two dimensional distributions in Fig.2.12a. It shows the y-residual versus strip-cluster position relative to the closest inter-strip gap center $y_{sTGC,0}^{rel}$. This effect is corrected using a sinusoidal function.

$$y_{sTGC} = y_{sTGC,0} - a_i \sin(2\pi y_{sTGC,0}^{rel}) \quad (2.1)$$

where $y_{sTGC,0}$ is the strip-cluster mean resulting from the Gaussian fit and y_{sTGC} is the corrected particle position estimator. The amplitude parameters are denoted a_i for the 3,4 and 5 strip-multiplicity (cluster size). These amplitude parameters are free parameters in the fit. The values of the amplitude parameters obtained from the fit to data are compatible with being equal for the three strip-cluster multiplicity as shown in table 2.2.

The correction function is therefore universal and is shown in Fig.2.12a. The two-dimensional distribution after the correction is applied was to be reasonably flat as shown in Fig.2.12b.

The alignment of the coordinate system of the pixel telescope with respect to the above-defined coordinate system of the sTGC layer also affects the measured residual distribution. A simple two-parameter model is used to account for translations and rotations of the two coordinate systems with respect to each other. Both the alignment correction and the differential non-linearity correction are included *in situ* in the analysis. The alignment correction is introduced in the model by expressing the pixel track position in the sTGC-layer coordinate system y_{pix} , is a function of the track position in the pixel telescope coordinate system x'_{pix} and y'_{pix} , and two misalignment parameters δy and ϕ_{xy} , as follows:

$$y_{pix} = -x'_{pix} \sin \phi_{xy} + y'_{pix} \cos \phi_{xy} + \delta y \quad (2.2)$$

The variable δy corresponds to a misalignment along the y-axis of the sTGC coordinate system, and ϕ_{xy} corresponds to a rotation of the telescope coordinate system in the x-y plane around the z-axis of the sTGC coordinate system. Translation and rotation misalignment along and around the other axis are not taken into account in this model, since they are expected to have a small impact on the determination of the intrinsic position resolution.

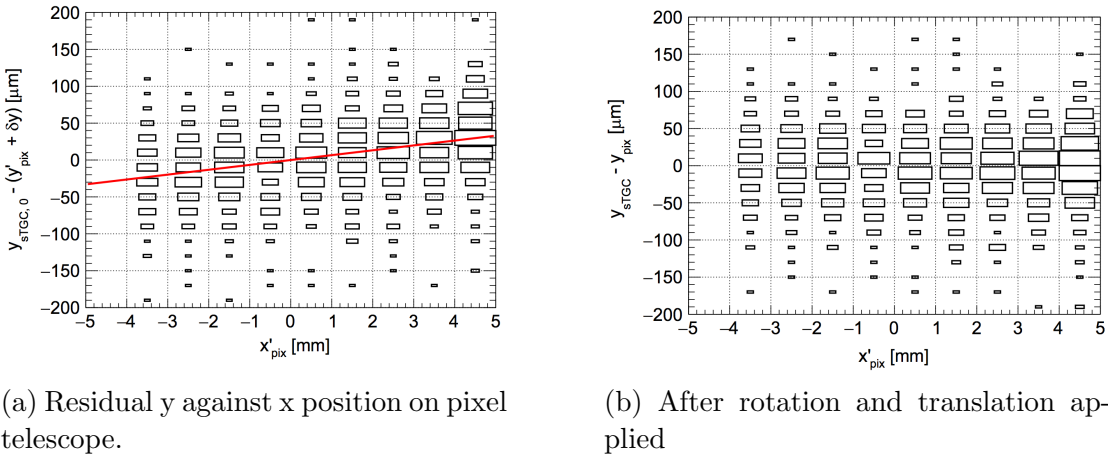


Figure 2.13: Coordinate system correction

On the figure 2.13a is possible to observe the y-residual mean increase linearly as a function of the x position on the telescope called x'_{pix} , which is evidence for a small rotation between the two coordinate systems. The red line represents the correction applied to this dataset. Accounting for this correction results in a distribution that is independent of x'_{pix} on figure 2.13b.

After all the corrections applied, the calculations for the intrinsic resolutions are taking each layer from the sTGC and comparing the residual distribution, and fitted by a double Gaussian function, where the first one represents the core of the residual distribution and the second is a wider Gaussian which represents some reconstructed strip-cluster from background sources.

$$\begin{aligned} F_i &= F_i(y_{sTGC,0}, y'_{sTGC,0}, x'_{pix}, y'_{pix}; \delta y, \phi_{xy}, a_i, \sigma, f, \sigma_w) \\ &= fG(y_{sTGC} - y_{pix}; 0, \sigma) + (1 - f)G(y_{sTGC} - y_{pix}; 0, \sigma_w) \end{aligned}$$

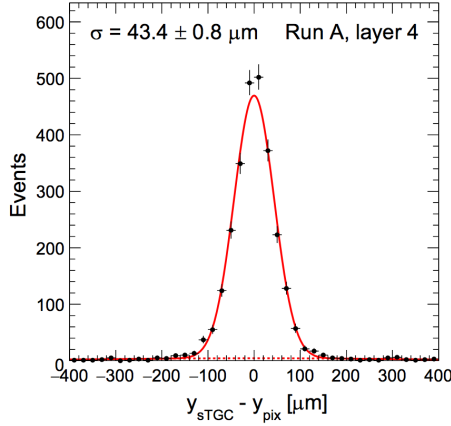
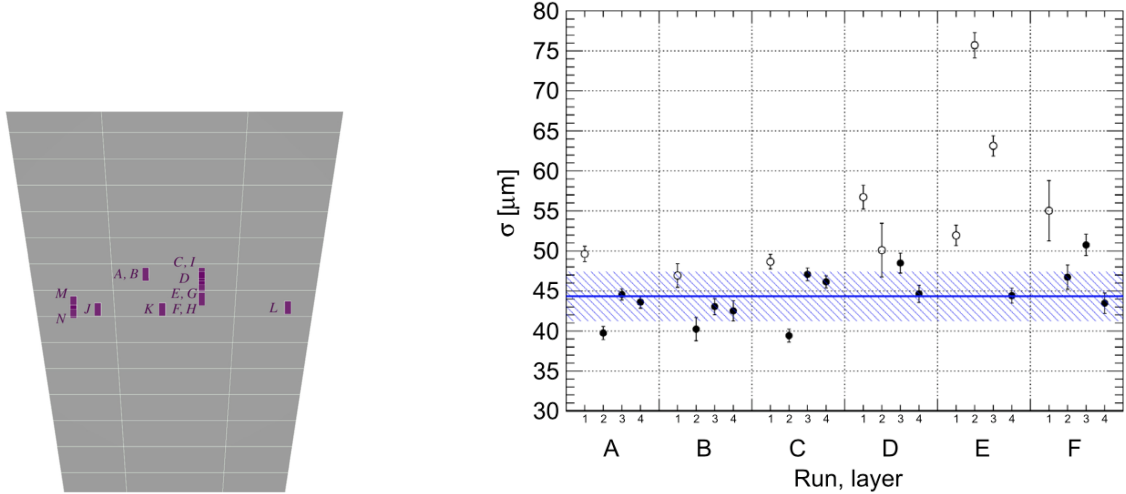


Figure 2.14: Intrinsic resolution of layer 4, respect to pixel telescope.

Figure 2.15: Summary of pixel telescope analysis

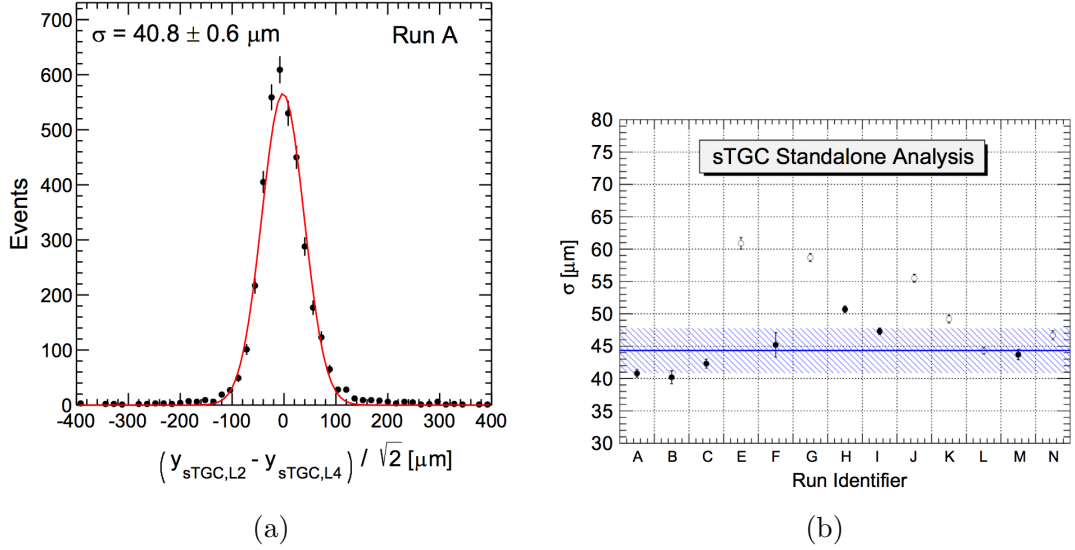


(a) Beam position for different data sets on sTGC

(b) Summary of intrinsic resolution for each data set and layer of sTGC

On figure 2.14 a set of events shows the distribution presented before with a intrinsic resolution parameter σ of about $44\mu\text{m}$ for a representative data taking run and sTGC strip-layer, where on red is the narrow Gaussian fit and on braking red line the wider Gaussian fit. The fraction of the data parameterized by the narrow Gaussian and it is typically around 95% with a RMS of about 2%. The rest of data taking runs and its beam position can be observe on figure 2.15, where the black circles represent the valid data and the open circles the runs with expected degradation due detector structure support or mis-calibrations.

sTGC standalone analysis



In this analysis the correction for the differential non-linearity respect to strip-pitch obtained before is kepted, however the residual distribution of the y-position is calculated from two pairwise layer of the sTGC, therefore half of the variance of this distribution correspond to our parameter to estimate the intrinsic resolution for one layer, hence $\sigma = \sigma_{\text{residual}}/\sqrt{2}$ and a strip-layer position residual distribution for a representative sTGC standalone data taking run is shown in figure 2.17a. In this graph, a intrinsic resolution of $\sigma = 40.8 \pm 0.8 \mu\text{m}$ is obtained.

In summary for fourteen data sets, the intrinsic resolution with this analysis is about $45 \mu\text{m}$. The white open circles on the graph 2.15 correspond to non-validate data due to wire-support position or mis-calibrations. The hash band represent the RMS spread and the blue line the average.

2.7. Pad efficiency

One of the new features of the small-strip Thin Gap Chamber compare to its previous version is the possibility to provide a fast trigger for the Region of Interest from the $8 \times 50 \text{ cm}^2$ pad area, where 3 out of 4 pads from a sTGC quadruplet can confirm a particle candidate, therefore a track position can be obtained from the strips within this area.

A test beam experiment was conducted at the CERN H6 facilities, using a 130 GeV muon beam of about 4 cm radius, a wider beam spot to test the characteristics of the pads. The setup is shown in figure 2.18 where the system was triggered by a set of scintillators (in blue) with a $12 \times 12 \text{ cm}^2$ coincidence area.

As explained before, for the beam tests a preliminary front-end electronics based on the VMM1 was used. This ASIC provide a Time-over-threshold signal as digital output, however is also possible to get a analog pulses. During the test beam, using the present

configuration an inefficiency was observed related to small late charges from the sTGC detector which may be not well adapted to the VMM1. An efficiency of 80-90% was observed running at 100 kHz/cm^2 .

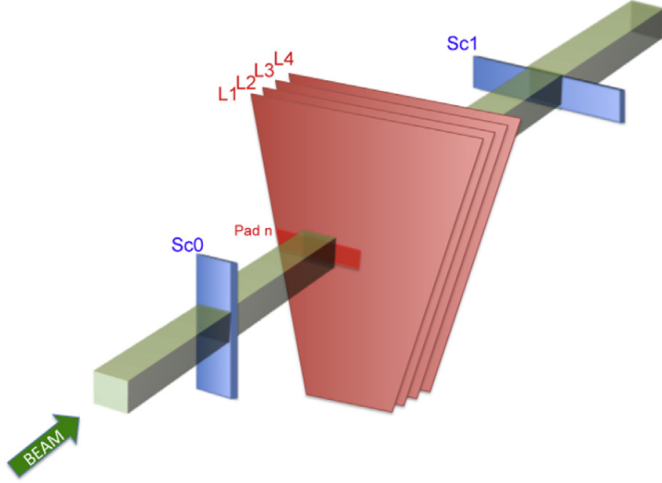
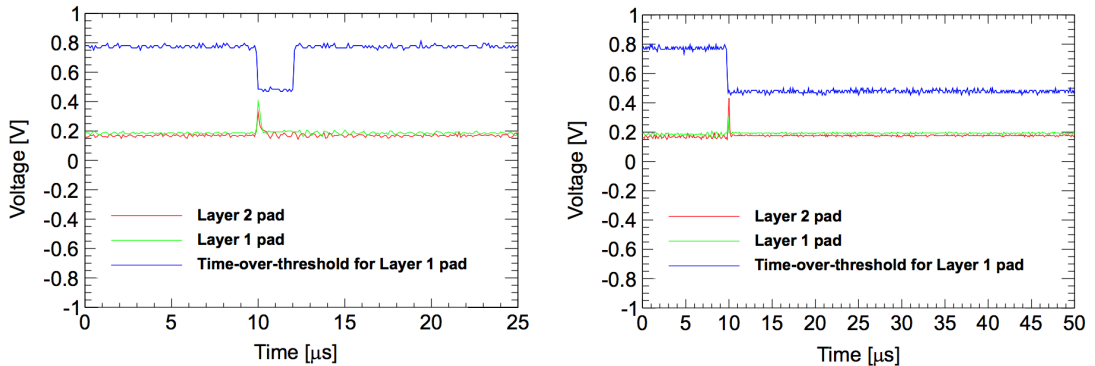


Figure 2.18: Setup for pad measurements, coincidence block on light green.

To ensure that no inefficiency was due to the detector itself, the large cathode pads were used to estimate the detector efficiency, which was measured by looking at the analog output of the front-end amplifier. The efficiency of the pad n in the first layer was defined with respect to the coincidence of the trigger with a signal in the fully overlapping pad of the second layer.



(a) ToT signal from pad L1, pad L2 as a trigger (b) Large dead time on ToT signal from pad L1

Figure 2.19: Digital and analog signal from VMM1

Two examples from this configuration are shown on figure 2.19, on the left a two analog signals from pads are present with a ToT signal from layer 1 with about $2\text{ }\mu\text{s}$ length, meanwhile on the right picture a long ToT pulse with more than $40\text{ }\mu\text{s}$ length

when the two analog signal are present. By recording hundreds of triggered events using an oscilloscope, the presence of a detector signal whithin the live-part of the front-end electronics (independent of the signal threshold) was checked. This test confirmed that the detector was 100% efficient.

charge sharing between pads

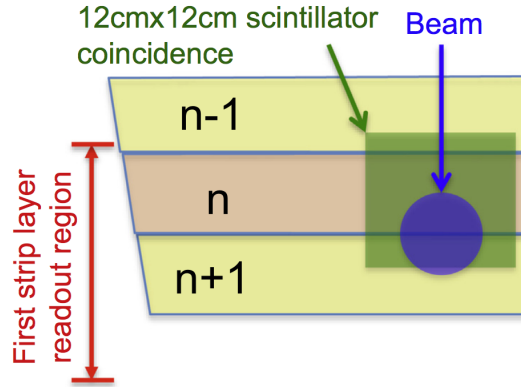


Figure 2.20: Pad region transition scheme

In manner to study the transition region between pads, the scintillator coincidence triggering area and the particle beam were centred between pad n and pad $n + 1$ of the first layer, as illustrated in Figure 2.20.

After applying timing quality requirements on the strip and pad hits, the channel baseline values are subtracted from the analog peak values. Strip-clusters with induced charge in either 3,4 or 5 adjacent strips are selected and calibrated in the same way as for the Fermilab beam test. Events with a single strip-cluster in the first layer and the second layer are selected. The strip-cluster position (mean of the fitted Gaussian) in the first layer is used to define the position of the particle going through the detector. The events are further required to contain a hit above threshold on either pad n or pad $n + 1$. The charge fraction (F) is defined using the analog peak values (P) of the two adjacent pads:

$$F = \frac{P_n - P_{n+1}}{P_n + P_{n+1}} \quad (2.3)$$

Figure 2.21 shows the charge fraction as a function of the position with respect to the centre of the transition region, where the two pads share more than 70% of the induced charge, spans about 4mm.

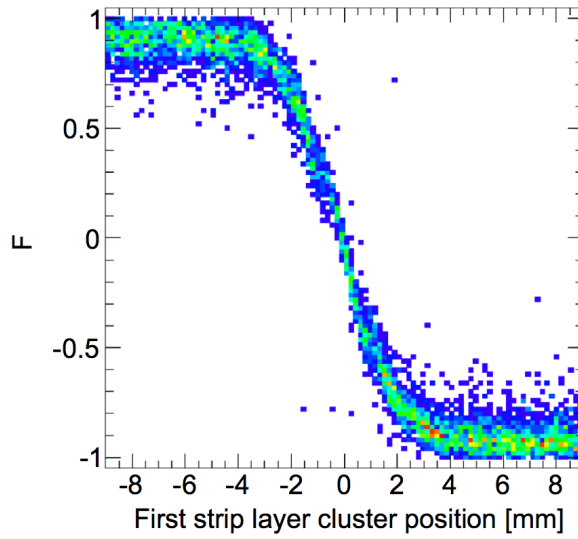


Figure 2.21: Charge Sharing distribution

2.8. Summary

Simulations, construction , calibrations, characterization of sTGC has been done. What's next? Test with cosmic rays for efficiency measurements, and test under hadron and muon beams with NSW electronic readout.

3. High count rate γ -ray spectroscopy with Brilliance380

3.1. Scintillators counters

- Introduction to Scintillators technologies.
- Scintillations mode and type of scintillators
- main characteristics
- Scintillator plus photomultiplier
- Brilliance 380

3.2. Counter Limit

Limit of pulse recognition, refer paper high rate...

3.3. Internal radiation

Show spectrum of Brilliance 380 and describe all the regions and peaks

3.4. High Radiation Source

Description of Cesium source, flow estimation for GIF++,

3.5. Data Analisys

Multiples pulses inside triggered window in scope
Pattern recognition?
Charge estimation

3.5.1. Multiple hits

how to handle it?

3.5.2. Wavelets

Introduction to Wavelets
Discrete Wavelet Transform

3.5.3. Peak identification

Choosing Wavelet function for peak identification
Heavy ion paper, peak identification

3.6. Results

Show multiple pulse in window, and peak identification, cases...

3.6.1. Spectrum

Spectrum for different rates (attenuation filters)
Spectrum with multiple pulse, using peak identification and pattern recognition.

3.6.2. Gamma Flux Rates

Rate estimation, compare with gain and rate measured with Scaler.

4. Synchrotron Radiation Detector for tagging electrons

4.1. NA64 experiment

The NA64 experiment is a fixed-target experiment at the CERN SPS combining the active beam dump and missing energy techniques to search for rare events.

A fully hermetic detector placed on the H4 beam line has been built with the primary goal to search for light dark bosons (Z') from dark sector that are coupled to photons, e.g. dark photons (A'), or sub-GeV Z' coupled only to quarks. In some cases the Z' is coupled only to μ or tau, so we call the Z' the dark leptonic gauge boson. The experiment is also capable to search for $K_L \rightarrow$ invisible decay, which is complementary to $K^+ \rightarrow \pi^+ + \nu\nu$, and invisible decays of π_0, η, η', K_S mesons.

The advantage of this approach is that the sensitivity (or number of signal events) of the experiment is roughly proportional to the Z' coupling squared ε^2 , associated with the Z' production in the primary interaction in the target/ While in a classical beam dump experiment, it is proportional to ε^4 , one ε^2 came from the Z' production, and another ε^2 is either from the probability of Z' decays or their interactions in a detector located at a large distance from the beam dump.

The sensitivities of these two methods depend on the region under study in the (ε^2, m_Z) parameter space, background level for a particular process, available beam intensity, etc. [Beam intensity] In some cases, much less running time and primary beam intensity are required to observe a signal event with our approach.

4.1.1. Physics Motivation

Standar Model.
g2 muon anomaly

4.1.2. Dark Photon signal

U(1) broken symmetry $-i$ massive dark photon
type of mixing coupling constant and subGeV mass connect with g2 muon anomaly. How

to detect him?

4.1.3. Particle identification

4.1.4. Setup

4.2. Synchroton Radiation Detector

4.2.1. BGO

4.2.2. Pb+Sc

4.2.3. LYSO

4.3. Calibration

4.4. Position and time resolution

4.5. Hadron rejection

4.6. Purity 100 GeV electron identification

4.7. Summary

5. Conclusion

A. Appendix

- A.1. Mechanical Measurements sTGC Module 0**
- A.2. PMT RT7525 Data Sheet**
- A.3. Data Structure NA64 Experiment**
- A.4. DAQ system**

Bibliography

- [1] G.Mikenberg. Thin-gas gap chambers for hadronic calorimetry. *Nucl. Instr. and Meth. A*, 265:223–227, 1988.
- [2] S.Majeski. A thin wire chamber operating in a high multiplication mode. *Nucl. Instr. and Meth A*, 217:265–271, 1983.
- [3] V.Smakhtin. Thin gap chamber upgrade for slhc: Position resolution in a test beam. *Nucl. Instr. and Meth. A*, 598:196–200, 2009.